

Reduction of surface spin-induced electron spin relaxations in nanodiamonds

Zaili Peng,¹ Jax Dallas,¹ and Susumu Takahashi^{1, 2, a)}

¹⁾*Department of Chemistry, University of Southern California, Los Angeles, California 90089, USA*

²⁾*Department of Physics & Astronomy, University of Southern California, Los Angeles, California 90089, USA*

(Dated: 11 August 2020)

Nanodiamonds (NDs) hosting nitrogen-vacancy (NV) centers are promising for applications of quantum sensing. Long spin relaxation times (T_1 and T_2) are critical for high sensitivity in quantum applications. It has been shown that fluctuations of magnetic fields due to surface spins strongly influences T_1 and T_2 in NDs. However, their relaxation mechanisms have yet to be fully understood. In this paper, we investigate the relation between surface spins and T_1 and T_2 of single-substitutional nitrogen impurity (P1) centers in NDs. The P1 centers located typically in the vicinity of NV centers are a great model system to study the spin relaxation processes of the NV centers. By employing high-frequency electron paramagnetic resonance (EPR) spectroscopy, we verify that air annealing removes surface spins efficiently and significantly reduces their contribution to T_1 .

^{a)}Electronic mail: susumu.takahashi@usc.edu

I. INTRODUCTION

Diamond is a fascinating material in physics, chemistry and biology. For example, a negatively charged nitrogen-vacancy (NV) center in diamond is a promising platform for fundamental sciences and applications of quantum sensing because of its unique magnetic and optical properties as well as a long coherence time at room temperature.¹⁻¹¹ Magnetic sensing using a single NV center has been utilized to improve the sensitivity of electron paramagnetic resonance (EPR) spectroscopy to the level of a single spin.¹²⁻²⁰ NV-detected EPR allows the detection of external spins existing around the NV center within several nanometers. NV-based sensing is also useful to detect electric field, temperature, strain and pH value in a nanoscale volume.²¹⁻²⁴ In NV-detected magnetic sensing, a magnetic field is detected through the measurement of the spin relaxation times of NVs such as T_2 and T_1 . For example, in NV-based AC magnetic sensing measurement using a spin echo sequence, the detectable magnetic field is proportional to $1/\sqrt{T_2}$.²⁵ A small number of Gd^{3+} spins has been detected through sensing of fluctuating magnetic fields from Gd^{3+} spins.¹⁴ In this case, the detection is achieved by measuring changes of T_1 relaxation time and the detectable magnetic field is proportional to $1/T_1$. Thus, long T_1 and T_2 times are desired for high detection sensitivity.

In NV-based magnetic sensing applications, it is also critical to position the NV center near a target of the magnetic field sensing. NVs located near the diamond surface and NVs in nanodiamonds (NDs) will therefore be an ideal platform for the applications. However, T_1 and T_2 relaxation times of those NVs are often significantly reduced by surface defects and impurities including dangling bonds, graphite layers and transition metals.^{14,17,26-36} For instance, it has been reported that shorter T_1 and T_2 were observed from shallow NVs.^{31,37} It has also been reported that T_1 of NVs in NDs is shorter than T_1 in bulk diamond. The recent study showed that T_1 of NV centers is shorter in a smaller size of NDs and the result implies a decoherence process due to surface impurities although the surface impurities were not measured in the study.¹⁴ Moreover, control of the diamond surface enables the determination of spin relaxation mechanisms, subsequently improving the sensitivity of the NV-based magnetic sensing techniques. The recent experiment by Tsukahara et al. showed that air annealing efficiently removes graphite layers compared with tri-acid cleaning and increases the T_2 time 1.4 times longer.³⁸

In this paper, we investigate the relation between surface spins and T_1 and T_2 of single substitutional nitrogen impurity (P1) centers in NDs using high-frequency (HF) EPR spectroscopy.

Our previous study on NDs suggested that the surface spins are dangling bonds located in the surface shell with a thickness of ~ 9 nm.³⁶ Therefore, the present study aims to remove the surface spins by etching of NDs more than 9 nm and improve the spin relaxation times. Although T_1 and T_2 of NV centers are the primary interest for the quantum sensing applications, there are a few advantages to study the spin relaxation on P1 centers over NV centers. First, NV centers are located near P1 centers, shown by the detection of their magnetic dipole coupling via double electron-electron resonance spectroscopy.^{12,20,39} Therefore, their T_1 and T_2 times are similar and the relaxation mechanisms are often common.⁶ Second, as shown in the previous study,³⁶ EPR signals of both P1 and surface spins are observable in the same measurement. This allows us to determine the amount of surface spins and to study the spin relaxations using the same ND samples. In the experiment, we employ air annealing to etch the diamond surface efficiently. The performance of the air annealing is confirmed by dynamic light scattering (DLS) and 230 GHz EPR experiments. The result of the DLS characterization shows a uniform etching and a linear etching rate of ND samples. We also confirm the reduction of the surface spins after the annealing process with high resolution 230 GHz EPR spectral analysis. Then, we investigate T_1 of P1 centers after the annealing using 115 GHz pulsed EPR spectroscopy. The 115 GHz EPR configuration is advantageous for pulsed EPR experiment because of its higher output power. The temperature and size dependence study elucidates surface spin-induced T_1 process. From the result, we find that air annealing significantly reduces the presence of surface spins, but a small fraction remains, even after the thickness of NDs is reduced more than 9 nm. We also find that the surface spin contribution on T_1 is suppressed by a factor of 7.5 ± 5.4 after annealing at 550 °C for 7 hours. With the same annealing condition, T_2 is improved by a factor of 1.2 ± 0.2 .

EPR signals of both P1 and surface spins are observable in the same measurement. This allows us to determine the amount of surface spins and to study the spin relaxations using sample samples. In the experiment, we employ air annealing to etch the diamond surface efficiently. The performance of the air annealing is confirmed by dynamic light scattering (DLS) and 230 GHz EPR experiments. The result of the DLS characterization shows a uniform etching and a linear etching rate of ND samples. We also confirm the reduction of the surface spins after the annealing process with high resolution 230 GHz EPR spectral analysis. Then, we investigate T_1 of P1 centers after the annealing using 115 GHz pulsed EPR spectroscopy. The 115 GHz EPR configuration is advantageous for pulsed EPR experiment because of its higher output power. The temperature and size dependence study elucidates surface spin-induced T_1 process. From the result, we find

that air annealing significantly reduces the presence of surface spins, but a small fraction remains, even after the thickness of NDs is reduced more than 9 nm. We also find that the surface spin contribution on T_1 is suppressed by a factor of 7.5 ± 5.4 after annealing at 550 °C for 7 hours. With the same annealing condition, T_2 is improved by a factor of 1.2 ± 0.2 .

II. MATERIALS AND METHODS

A. Nanodiamond

Five different sizes of diamond powders were investigated in the present study. The samples include micron-sized diamond powders ($10 \pm 1 \mu\text{m}$) (Engis Corporation), and four different sizes of NDs (Engis Corporation and L.M. Van Moppes and Sons SA). The mean diameters of the ND samples specified by the manufacturers are $550 \pm 100 \text{ nm}$, $250 \pm 80 \text{ nm}$, $100 \pm 30 \text{ nm}$, and $50 \pm 20 \text{ nm}$. All diamond powders were manufactured by mechanical milling or grinding of type-Ib diamond crystals. The concentration of nitrogen related impurities in the ND powders is in the order of 10 to 100 parts per million (ppm) carbon atoms.

B. Air annealing

The air annealing process was performed using a tube furnace (MTI Corporation) where a ND sample was positioned in a quartz tube located in the cylindrical access of the furnace. For the preparation of the annealing process, the ND sample was placed in a 5 ml of acetone. The ND sample in acetone was then mixed by utilizing ultrasound sonication for 10 min at room temperature in order to achieve uniform dispersion. After the ultrasound sonication, the sample solution was placed in a crucible and kept in a fume hood overnight (without application of heating) in order to evaporate acetone from the crucible. In the air annealing process, the temperature of the furnace was first stabilized at the annealing temperature (550 °C in the present case), and then the ND sample in the crucible was inserted at the center of the quartz tube. In order to improve homogeneity of the application of the air annealing over the ND powders, the NDs were mixed by a lab spatula periodically during the annealing (typically mixed for 30 seconds every 10 minutes). We also limited the initial amount of ND samples to be approximately 30 mg for the homogeneous application of the air annealing.

C. Dynamic light scattering

The size of a diamond powder sample was characterized by dynamic light scattering (DLS) (Wyatt Technology). A diamond powder sample of ~ 1 mg was suspended in methanol and sonicated for two hours before the measurement of DLS. The DLS measurement was performed with a 632 nm incident laser and 163.5° of detection angle. The second correlation data was analyzed using the constrained regularization method to obtain particle sizes.

D. HF EPR spectroscopy

HF (230 GHz and 115 GHz) EPR experiments were performed using a home-built system at University of Southern California. The HF EPR spectrometer consists of a high-frequency high-power solid-state source, quasi-optics, a corrugated waveguide, a 12.1 Tesla superconducting magnet, and a superheterodyne detection system. The output power of the source system is 100 mW at 230 GHz and 480 mW at 115 GHz, respectively. A sample on a metallic end-plate at the end of the corrugated waveguide is placed at the center of the 12.1 Tesla EPR superconducting magnet. Details of the system have been described elsewhere.⁴⁰ In the present study, the diamond powder sample was placed in a Teflon sample holder (5 mm diameter), typically containing the diamond powders of 5 mg.⁴¹ For cw EPR experiments, the microwave power and magnetic field modulation strength were adjusted to maximize the intensity of EPR signals without distortion of the signals.³⁶ A typical modulation amplitude was 0.02 mT at a modulation frequency of 20 kHz.

III. RESULTS AND DISCUSSION

We employed air annealing for the removal of the surface spins in the present study. In the air annealing the surface removal is caused by etching by oxygen where oxygen molecules oxidize carbon and form gaseous CO and CO₂. We first compared the weight of the ND sample before and after the annealing process. Figure 1(a) shows the ND normalized weight as a function of the annealing time. In the experiment, the annealing was done at an annealing temperature of 550 °C. The result shows linear reduction in ND weight with increased annealing time. The size of the ND samples was then characterized using DLS. As shown in Fig. 1(b), the ND size decreased from $d_{peak} = 53.4$ nm to 22.4 nm after the annealing for 9 hours. The observed reduction and narrow distribution of the size indicates a successful and uniform application of the annealing to

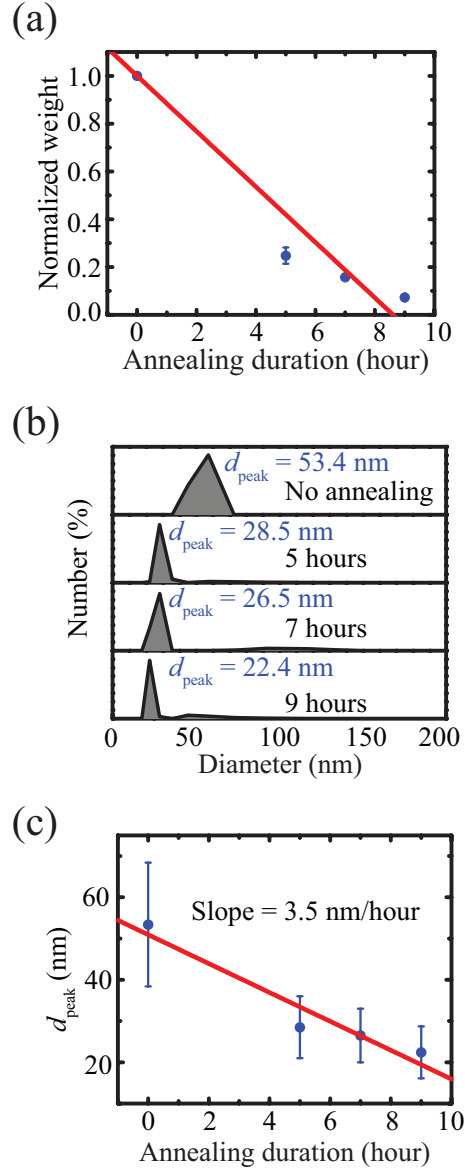


FIG. 1. Overview of the air annealing experiment. (a) The normalized weight as a function of the annealing duration with annealing at 550 °C. The red solid line shows a linear fit to obtain the rate of weight reduction. The weight reduction rate was 0.12 hour^{-1} . Each sample was weighed five times. The error bar represents the standard deviation of the measurements. (b) DLS results for the size characterization of the ND samples before and after the annealing for 5, 7 and 9 hours. The diameter at the maximum in the distribution (d_{peak}) is indicated. The obtained polydispersity index (PDI) were 0.11, 0.07, 0.06 and 0.08 for the no-annealing sample and the annealing for 5, 7 and 9 hours samples, respectively. (c) d_{peak} as a function of the annealing duration. The red solid line represents the result of a linear fit. The error bar represent the standard deviation (calculated by $d_{peak}\sqrt{PDI}$).

NDs. Figure 1(c) shows the ND size as a function of the annealing duration. We observed a linear relationship between the size reduction and the annealing duration. A reduction rate of 3.5 nm/hour was obtained from the linear fit.

Next, we characterized paramagnetic spins existing in NDs using 230 GHz EPR spectroscopy. Figure 2(a) shows 230 GHz continuous-wave EPR spectra on 50-nm ND samples before and after the air annealing. The measurements were performed at room temperature. As shown in Fig. 2(a), all spectra contain a pronounced and broad EPR signal at 8.206 Tesla and a narrow EPR signal at ~ 8.207 Tesla. From the EPR spectral analysis shown in the inset of Fig. 2(a), we identified that the EPR signal at 8.207 Tesla is from P1 centers while the signal at 8.206 Tesla is from the surface spins (dangling bonds). The result is consistent with the previous HF EPR study.³⁶ As shown in Fig. 2(a), the intensity of the EPR signals from the surface spins decreases significantly after the annealing. In general, the EPR intensity is related to the spin population, we therefore analyzed the EPR intensity ratio between the surface spins (I_S , where S represents surface spins) and P1 (I_{P1}) to determine their spin population ratio. For example, we obtained I_S/I_{P1} to be 61 and 5 with no annealing and 9 hour annealing, respectively. The result from the EPR intensity and DLS analyses was summarized in Fig. 2(b). Since our previous HF EPR study of the non-annealed NDs showed the core-shell structure with the shell thickness (t) of 9 nm,³⁶ we first consider the core-shell model to understand the size dependence of the EPR intensity. In the core-shell model, the EPR intensity ratio,

$$\left(\frac{I_X}{I_{P1}}\right)_{coreshell} = \frac{\rho_X V_X}{\rho_{P1} V_{P1}} = \frac{\rho_X [4\pi/3\{(d/2)^3 - (d/2 - t)^3\}]}{\rho_{P1} [4\pi/3(d/2 - t)^3]},$$

where ρ_X (ρ_{P1}) is the density of the surface spins (P1 spins) and V_X (V_{P1}) is the volume of the surface spin (P1 spin) locations. The calculated $(I_S/I_{P1})_{coreshell}$ is shown in Fig. 2(b). However, we observed a poor agreement with the experimental data in the range of $d < 35$. There may be two possible reasons to explain the result. First, as reported previously⁴²⁻⁴⁶, the etching rate of the air annealing depends on a crystallographic axis. It has been shown that the etching rate of the (111) plane is a couple of times faster than the (100) plane.⁴⁷ However, this can explain only the dependence of EPR, but not the dependence of DLS. Another possible reason is the creation of a small amount of surface spins during air annealing. For instance, it has been reported that dangling bonds were created by air annealing, especially when the surface termination was dominated by C-H bonds.⁴⁸ In the latter scenario, the surface spins in the non-annealed NDs (dangling bonds) are located in the shell, and then air annealing removes the dangling bonds in the shell as well as

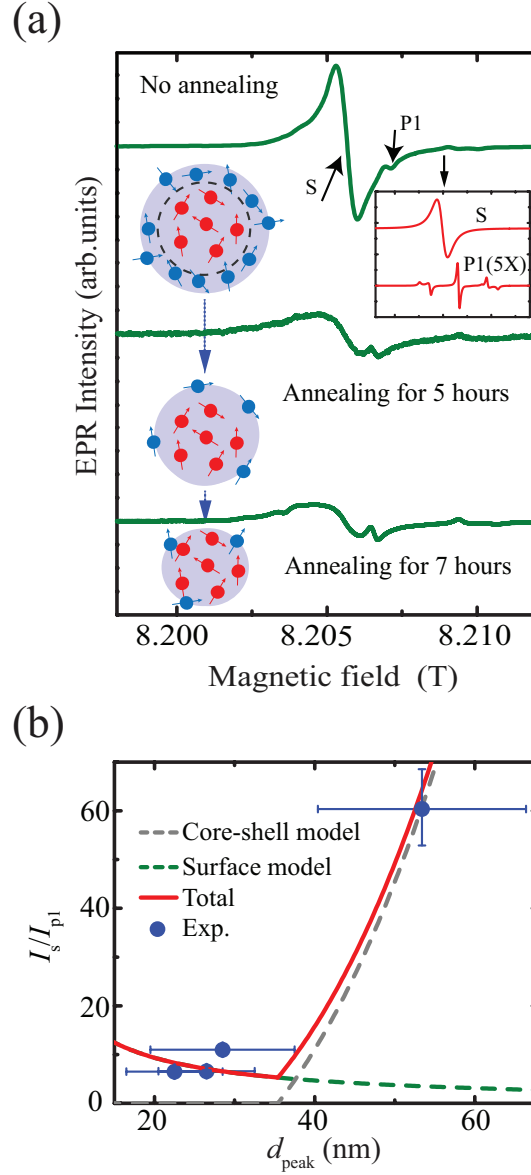


FIG. 2. cw EPR analysis of 50-nm NDs before and after the air annealing. (a) Signal intensity as a function of magnetic fields in Tesla with no annealing, annealing for 5 hours and 7 hours. The solid green lines represent the experimental data. The inset on the top right shows contributions of P1 and surface spins (S) on the EPR spectrum, which were extracted from the EPR spectral analysis. Drawings representing NDs under the annealing process are also shown in the inset. The red arrows in the drawing represent the P1 centers, and the blue arrows represent surface spins. (b) The EPR intensity ratio I_s/I_{P1} as a function of the diameter (d_{peak}). The blue solid circles with error bars represent I_s/I_{P1} obtained from EPR spectral analysis. The details of the EPR spectral analysis is described in Supplementary Material. The gray dashed line is the simulated $(I_s/I_{P1})_{coreshell}$. The green dashed line is the simulated $(I_s/I_{P1})_{surface}$.

creates a small amount of dangling bonds on the surface (see Fig. 2(a)). To take into account the surface spins created by air annealing, we added a contribution from the surface spin model with which,

$$\left(\frac{I_X}{I_{P1}}\right)_{surface} = \frac{\rho_s[4\pi(d/2)^2]}{\rho_{P1}[4\pi/3(d/2)^3]} \propto \frac{\rho_s}{d}.$$

ρ_s is the surface spin density, treating as a constant here. As shown in Fig. 2(b), the sum of the core-shell and surface models agrees with the experimental result, supporting the latter case.

TABLE I. Summary of T_1 analyses. For the Γ_s analysis, Eq. 1 and $C = 2.96 \times 10^{-10}$ ($s^{-1}K^{-5}$) were used. T_1 and Γ_s are shown with three significant figures. The errors in T_1 represent the standard error of the mean. The errors in Γ_s were calculated as the 95% confidence interval.

Sample	T_1 (ms)					Γ_s (s^{-1})
	100 K	150 K	200 K	250 K	300 K	
50 nm	0.581 ± 0.339	0.519 ± 0.341	0.382 ± 0.080	0.132 ± 0.034	0.320 ± 0.020	2430 ± 650
100 nm	1.74 ± 0.12	1.68 ± 0.18	1.19 ± 0.23	1.02 ± 0.15	0.668 ± 0.141	587 ± 63
250 nm	25.6 ± 1.2	19.3 ± 0.7	7.80 ± 0.20	2.14 ± 0.07	1.26 ± 0.03	34.0 ± 16.9
550 nm	84.9 ± 7.4	42.5 ± 2.2	10.3 ± 0.4	2.58 ± 0.03	1.35 ± 0.03	8.12 ± 22.03
10 μm	1200 ± 580	62.2 ± 5.0	12.0 ± 0.4	3.15 ± 0.06	1.36 ± 0.03	—
Annealed (5h)	2.46 ± 0.50	1.41 ± 0.26	1.31 ± 0.35	0.885 ± 0.188	0.679 ± 0.240	531 ± 217
Annealed (7h)	4.37 ± 1.37	1.86 ± 0.48	1.37 ± 0.57	1.06 ± 0.27	0.847 ± 0.595	325 ± 217

Next, we measured the spin relaxation times (T_1 and T_2) of the ND samples. The experimental results of the 50-nm ND sample is shown in Fig. 3(a). The measurements of the T_1 and T_2 relaxation times of P1 centers were carried out using the inversion recovery and the spin echo sequences, respectively. The T_1 and T_2 measurements of P1 centers were performed at a microwave frequency of 115 GHz and 4.103 Tesla, corresponding to the center peak of the P1 EPR spectrum. By fitting the change of the spin echo intensity with a single exponential function, we obtained T_1 to be 0.382 ± 0.080 ms, and T_2 is 0.413 ± 0.007 μs as shown in the inset of Fig. 3(a) (see Supplementary Material for the description of the T_1 and T_2 determination). Moreover, we measured temperature dependence of T_1 and T_2 . Figure 3 (b) and Table I summarize the result of the T_1 measurements as a function of temperature. We observed that T_1 times increase drastically by decreasing temperature. In addition, the temperature dependence is strongly correlated with the size

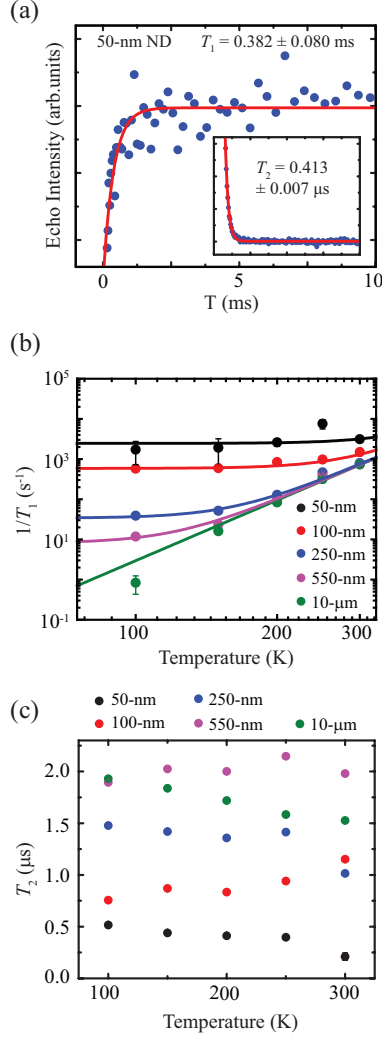


FIG. 3. Temperature dependence of T_1 and T_2 of P1 centers in NDs. (a) The T_1 measurement using the inversion recovery measurement. The measurement was performed at 200 K. The pulse sequence is $P_\pi - T - P_{\pi/2} - \tau - P_\pi - \tau - \text{echo}$ where $P_{\pi/2}$ and P_π are $\pi/2$ - and π -pulses, respectively, τ is a fixed evolution time and an evolution time T is varied in the measurement. In the measurement, the pulse lengths of $P_{\pi/2}$ and P_π were 300 ns and 500 ns, $\tau = 1.2 \mu\text{s}$ and the repetition time was = 10 ms. The inset shows the spin echo measurement at 200 K to obtain T_2 . The pulse sequence is $P_{\pi/2} - \tau - P_\pi - \tau - \text{echo}$ where τ is varied in the measurement. The pulse parameters for the T_2 measurement were $P_{\pi/2} = 300$ ns, $P_\pi = 500$ ns and the repetition time = 10 ms. The errors associated with T_1 and T_2 were obtained by computing the standard error. (b) Temperature dependence of $1/T_1$ on various sizes of NDs. The solid circles are experimental data and the solid lines are fits using Eq. (1). (c) T_2 on various sizes of NDs. The error bars are smaller than the dots representing the T_2 value.

of the diamond powder. To understand the temperature dependence, we first considered a contribution of the spin-lattice relaxation observed in bulk diamond. According to the previous studies of T_1 of bulk diamond, the temperature dependence of T_1 is well explained by a spin-orbit induced tunneling model,^{6,49} in which a spin flip event occurs due to the tunneling between P1's molecular axis orientations. Using the spin-orbit induced tunneling model, we write that $1/T_1$ is proportional to T^5 , namely, $1/T_1 = CT^5$, where the T -linear term in the spin-orbit induced tunneling model⁴⁹ is omitted because of its negligible contribution in the present temperature range.

By fitting the experimental data of the 10- μm diamond to the T^5 model, we obtained $C = (2.96 \pm 0.52) \times 10^{-10} \text{ s}^{-1} \text{ K}^{-5}$, which is in a good agreement with previous finding.^{6,49} The result was obtained from a weighted fit analysis in order to take into account the uncertainty in T_1 values (See Supplementary Material for the details). Furthermore, in cases of smaller diamond samples (from 550-nm to 50-nm NDs in Fig. 3(b)), we observed a strong deviation from the T^5 model and found that $1/T_1$ at low temperatures highly correlates with the size of NDs. Recent investigation of shallow NV centers as well as NV centers in a single ND showed that T_1 in NDs is attributed to surface spins.^{14,17,30,31} Since the surface spins were also detected from the same ND samples in our experiment, it is likely that the surface spins also influence T_1 of P1 centers in NDs. In order to take into account relaxation processes from both the surface spins and the spin-orbit induced tunneling, we consider the following for $1/T_1$,

$$\frac{1}{T_1} = CT^5 + \Gamma_s, \quad (1)$$

where Γ_s is the $1/T_1$ contribution from surface spins, originated by fluctuations of the magnetic dipole fields from the surface spins. Γ_s is assumed to be independent of temperature in a temperature range of the present experiment. In this $1/T_1$ model, when temperature increases, the first term (the spin-orbit induced tunneling contribution) increases. Therefore, when a sample has a significant contribution from the surface spin relaxation, $1/T_1$ has less pronounced temperature dependence. We performed a weighted fit analysis on 50-nm, 100-nm, 250-nm and 550-nm ND samples to determine their Γ_s (See Supplementary Material for the details). As shown in Fig 3 (b), we found a good agreement between the temperature dependence of $1/T_1$ and the model. For example, we obtained that Γ_s of the 50-nm ND sample was $2430 \pm 650 \text{ s}^{-1}$.

Furthermore, we investigated the temperature- and size-dependence of T_2 relaxation time of P1 centers. In contrast to the result of T_1 , T_2 of P1 centers in the studied NDs does not show noticeable temperature dependence (see Fig. 3(c)). Table II shows the summary of the temperature- and size-

TABLE II. Summary of T_2 analyses. T_2 and $\overline{T_2}$ are represented by three significant figures. The errors in T_2 represent the standard error of the mean. The errors in $\overline{T_2}$ were calculated as the 95% confidence interval.

Sample	T_2 (μs)					$\overline{T_2}$ (μs)
	100 K	150 K	200 K	250 K	300 K	
50 nm	0.518 ± 0.002	0.440 ± 0.002	0.413 ± 0.007	0.398 ± 0.008	0.211 ± 0.036	0.474 ± 0.060
100 nm	0.756 ± 0.007	0.871 ± 0.011	0.835 ± 0.017	0.942 ± 0.020	1.15 ± 0.01	0.882 ± 0.214
250 nm	1.48 ± 0.01	1.42 ± 0.01	1.36 ± 0.01	1.41 ± 0.01	1.02 ± 0.01	1.34 ± 0.23
550 nm	1.89 ± 0.02	2.03 ± 0.01	2.00 ± 0.01	2.15 ± 0.01	1.98 ± 0.01	2.03 ± 0.10
10 μm	1.93 ± 0.02	1.84 ± 0.02	1.72 ± 0.01	1.59 ± 0.01	1.53 ± 0.01	1.65 ± 0.17
Annealed (5hr)	0.510 ± 0.091	0.957 ± 0.208	0.341 ± 0.252	0.551 ± 0.208	0.869 ± 0.095	0.675 ± 0.274
Annealed (7hr)	0.520 ± 0.041	0.509 ± 0.036	0.634 ± 0.051	0.604 ± 0.015	0.600 ± 0.023	0.589 ± 0.048

dependence of T_2 as well as the mean T_2 ($\overline{T_2}$) which was obtained from a weighted fit analysis in order to take into account the errors in the T_2 values (See Supplementary Material for the details of the $\overline{T_2}$ analysis). $\overline{T_2}$ for 50-nm ND and 550-nm samples were $0.474 \pm 0.060 \mu\text{s}$ and $2.03 \pm 0.10 \mu\text{s}$, respectively. Therefore, T_2 of the 50-nm NDs is approximately 4.3 times shorter than that of 550-nm NDs. The result indicates the effect of the surface spins on T_2 . On the other hand, T_2 of 550-nm and 10- μm are similar ($\sim 2 \mu\text{s}$). This is probably because couplings to neighboring P1 centers dominates their T_2 processes.

Finally, we study the spin relaxation times (T_1 and T_2) of the annealed NDs. As shown in Fig. 4(a), T_1 times in the annealed diamond became longer after the annealing in the measured temperature range. In addition, as shown in Fig. 4(a), the T_1 times of the annealed NDs are still shorter than that of bulk diamond, implying the existence of remaining surface spins. To extract the contribution of the surface spins, we employed Eq. (1) to determine Γ_s . From the analysis, we indeed found that Γ_s in the annealed NDs are smaller than that of the non-annealed samples. The obtained Γ_s are $531 \pm 217 \text{ s}^{-1}$ and $325 \pm 217 \text{ s}^{-1}$ for the NDs annealed at 550°C for 5 hours and 7 hours, respectively, which are 4.6 ± 2.2 and 7.5 ± 5.4 times smaller than that of the non-annealed 50-nm NDs as shown in Fig. 4(b) (see Supplementary Material for the calculation of the Γ_s improvement factor).

We next discuss a model of the surface spin-induced T_1 (Γ_s). As reported previously,^{14,30,50}

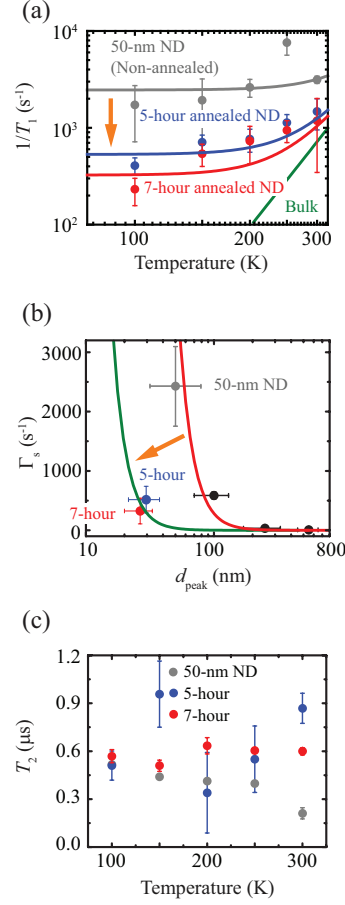


FIG. 4. Temperature dependence of T_1 and T_2 of P1 centers in the annealed ND samples (initial diameter = 50 nm). (a) T_1 of the annealed ND samples as a function of temperature. Experimental data points are indicated by blue circles and red triangles for air annealing at 550 °C for 5 hours and 7 hours, respectively. The blue and red solid lines are corresponding fits utilizing Eq. (1). T_1 data with no annealing (gray solid line) and the data of a bulk diamond (green solid line) are shown. The arrow represents the reduction of Γ_s . (b) Γ_s as a function of the ND diameter. The red solid line shows the fit result to the ρ_s/d^4 model for NDs without annealing. The green solid line shows the ρ_s/d^4 line simulated for the annealed NDs. The orange arrow represents the reduction of Γ_s . The error bar in the Γ_s is included and obtained by computing the 95 % confidence interval. (c) T_2 as a function of temperature for the non-annealed and annealed samples.

by considering fluctuating magnetic fields (B_{dip}) from surface spins, Γ_s is proportional to the variance ($\langle B_{dip}^2 \rangle$) and the spin density (ρ_s). By assuming that surface spins cover the whole surface uniformly, $B_{dip}^2(\vec{r}_{P1}) \propto \int_S \rho_s b_{dip}^2(\vec{r} - \vec{r}_{P1}) dS$, where the radius vectors (\vec{r} and \vec{r}_{P1}) define the locations of the surface and P1 spins relative to the center of the ND, respectively. $b_{dip}(\vec{r})$ is

the magnetic dipole field from the surface spins. By taking into account the quantization axis of P1 and the surface spins along the external magnetic field and considering a spherical shape of NDs and a spatially uniform ρ_s , $b_{dip}^2(\vec{r})$ is proportional to $1/d^6$ and the surface integral is proportional to d^2 , where d is a diameter of a ND, the magnetic field fluctuations ($B_{dip}^2(\vec{r})$) is therefore proportional to ρ_s/d^4 and Γ_s is also proportional to ρ_s/d^4 . The Γ_s values obtained from the temperature dependence T_1 in Fig. 3(b) were plotted as a function of the ND size in Fig. 4(b). We found a good agreement between the obtained Γ_s value and the $1/d^4$ size dependence. Thus, the result supports the T_1 relaxation mechanism in NDs due to the surface spins. Furthermore, as shown in Fig. 4(b), Γ_s of the annealed NDs are very different from the $1/d^4$ line of the non-annealed NDs, indicating significant reduction of the surface spin density. Using the same model ($\Gamma_s \propto \rho_s/d^4$), we estimated that ρ_s for the annealed NDs is ~ 100 times smaller than that of the non-annealed NDs (Fig. 4(b)).

In addition the T_2 of the annealed diamond was studied. As shown in Fig. 4(c), similarly to the non-annealed NDs, T_2 of the annealed diamond showed no temperature dependence. The mean T_2 times were $0.675 \pm 0.274 \mu\text{s}$ and $0.589 \pm 0.048 \mu\text{s}$ after the 5 and 7 hour annealing, respectively, showing that the extension of T_2 by a factor of 1.4 ± 0.6 and 1.2 ± 0.2 , respectively (see Supplementary Material for the calculation of the T_2 improvement factor). This improvement is due to the reduction of the surface spins. The observed T_2 improvement is comparable with the previously reported result.³⁸ By considering the T_2 results of the non-annealed NDs, we speculate that the T_2 relaxation in the annealed NDs is caused by couplings to residual surface spins and P1 centers.

IV. SUMMARY

In summary, we investigated the relationship between the surface spins and the spin relaxation times (T_1 and T_2) of P1 centers in NDs. We reduced the amount of the surface spins using air annealing. The amount of the surface spins was characterized by HF EPR analysis. The pulsed HF EPR experiment extracted the contribution of the surface spins on the T_1 relaxation successfully. We found clear correlation between the amount of the surface spins and T_1 . In addition, the present study showed the improvement of T_1 and T_2 by removing the surface spins. The finding of the present investigation sets the basis to suppress the spin relaxation process due to the surface spins in NDs which is critical for NV-based sensing applications. The present method is also potentially

applicable to improve spin and optical properties of other nanomaterials.

V. SUPPLEMENTARY MATERIAL

See the supplementary material for the T_1 and T_2 determination method, the EPR spectral analysis and the analyses of the temperature- and size-dependent T_1 and T_2 .

ACKNOWLEDGMENTS

We thank Benjamin Fortman for useful discussion of the EPR data analyses. This work was supported by the National Science Foundation (DMR-1508661 and CHE-1611134), the USC Anton B. Burg Foundation and the Searle scholars program. This material is also based upon work supported by the Chemical Measurement and Imaging program in the National Science Foundation Division of Chemistry under Grant No. CHE-2004252 (with partial co-funding from the Quantum Information Science program in the Division of Physics) (ST).

DATA AVAILABILITY STATEMENT

The data that support the findings of this study are available from the corresponding author upon reasonable request.

REFERENCES

- ¹A. Gruber, A. Dräbenstedt, C. Tietz, L. Fleury, J. Wrachtrup, and C. Von Borczyskowski, “Scanning confocal optical microscopy and magnetic resonance on single defect centers,” *Science* **276**, 2012 (1997).
- ²J. Wrachtrup and F. Jelezko, “Processing quantum information in diamond,” *J. Phys. Condens. Matter* **18**, S807 (2006).
- ³R. J. Epstein, F. M. Mendoza, Y. K. Kato, and D. D. Awschalom, “Anisotropic interactions of a single spin and dark-spin spectroscopy in diamond,” *Nat. Phys.* **1**, 94 (2005).
- ⁴T. Gaebel, M. Domhan, I. Popa, C. Wittmann, P. Neumann, F. Jelezko, J. R. Rabeau, N. Stavrias, A. D. Greentree, S. Praver, J. Meijer, J. Twamley, P. R. Hemmer, and J. Wrachtrup, “Room-temperature coherent coupling of single spins in diamond,” *Nat. Phys.* **2**, 408 (2006).

- ⁵L. Childress, M. V. G. Dutt, J. M. Taylor, A. S. Zibrov, F. Jelezko, J. Wrachtrup, P. R. Hemmer, and M. D. Lukin, “Coherent dynamics of coupled electron and nuclear spin qubits in diamond,” *Science* **314**, 281 (2006).
- ⁶S. Takahashi, R. Hanson, J. van Tol, M. S. Sherwin, and D. D. Awschalom, “Quenching spin decoherence in diamond through spin bath polarization,” *Phys. Rev. Lett.* **101**, 047601 (2008).
- ⁷C. L. Degen, “Scanning magnetic field microscope with a diamond single-spin sensor,” *Appl. Phys. Lett.* **92**, 243111 (2008).
- ⁸J. R. Maze, P. L. Stanwix, J. S. Hodges, S. Hong, J. M. Taylor, P. Cappellaro, L. Jiang, M. G. Dutt, E. Togan, A. Zibrov, *et al.*, “Nanoscale magnetic sensing with an individual electronic spin in diamond,” *Nature* **455**, 644 (2008).
- ⁹G. Balasubramanian, I. Y. Chan, R. Kolesov, M. Al-Hmoud, J. Tisler, C. Shin, C. Kim, A. Wojcik, P. R. Hemmer, A. Krueger, T. Hanke, A. Leitenstorfer, R. Bratschitsch, F. Jelezko, and J. Wrachtrup, “Nanoscale imaging magnetometry with diamond spins under ambient conditions,” *Nature* **455**, 648 (2008).
- ¹⁰L. T. Hall, J. H. Cole, C. D. Hill, and L. C. Hollenberg, “Sensing of fluctuating nanoscale magnetic fields using nitrogen-vacancy centers in diamond,” *Phys. Rev. Lett.* **103**, 220802 (2009).
- ¹¹P. Maletinsky, S. Hong, M. S. Grinolds, B. Hausmann, M. D. Lukin, R. L. Walsworth, M. Loncar, and A. Yacoby, “A robust scanning diamond sensor for nanoscale imaging with single nitrogen-vacancy centres,” *Nat. Nanotechnol.* **7**, 320 (2012).
- ¹²G. de Lange, T. van der Sar, M. Blok, Z.-H. Wang, V. Dobrovitski, and R. Hanson, “Controlling the quantum dynamics of a mesoscopic spin bath in diamond,” *Sci. Rep.* **2**, 382 (2012).
- ¹³M. S. Grinolds, S. Hong, P. Maletinsky, L. Luan, M. D. Lukin, R. L. Walsworth, and A. Yacoby, “Nanoscale magnetic imaging of a single electron spin under ambient conditions,” *Nat. Phys.* **9**, 215 (2013).
- ¹⁴J.-P. Tetienne, T. Hingant, L. Rondin, A. Cavaillès, L. Mayer, G. Dantelle, T. Gacoin, J. Wrachtrup, J.-F. Roch, and V. Jacques, “Spin relaxometry of single nitrogen-vacancy defects in diamond nanocrystals for magnetic noise sensing,” *Phys. Rev. B* **87**, 235436 (2013).
- ¹⁵H. Mamin, M. Kim, M. Sherwood, C. Rettner, K. Ohno, D. Awschalom, and D. Rugar, “Nanoscale nuclear magnetic resonance with a nitrogen-vacancy spin sensor,” *Science* **339**, 557 (2013).
- ¹⁶M. S. Grinolds, M. Warner, K. De Greve, Y. Dovzhenko, L. Thiel, R. L. Walsworth, S. Hong, P. Maletinsky, and A. Yacoby, “Subnanometre resolution in three-dimensional magnetic reso-

- nance imaging of individual dark spins,” *Nat. Nanotechnol.* **9**, 279 (2014).
- ¹⁷S. Kaufmann, D. A. Simpson, L. T. Hall, V. Perunicic, P. Senn, S. Steinert, L. P. McGuinness, B. C. Johnson, T. Ohshima, F. Caruso, *et al.*, “Detection of atomic spin labels in a lipid bilayer using a single-spin nanodiamond probe,” *Proc. Natl. Acad. Sci.* **110**, 10894 (2013).
- ¹⁸A. O. Sushkov, I. Lovchinsky, N. Chisholm, R. L. Walsworth, H. Park, and M. D. Lukin, “Magnetic resonance detection of individual proton spins using quantum reporters,” *Phys. Rev. Lett.* **113**, 197601 (2014).
- ¹⁹F. Shi, Q. Zhang, P. Wang, H. Sun, J. Wang, X. Rong, M. Chen, C. Ju, F. Reinhard, H. Chen, J. Wrachtrup, J. Wang, and J. Du, “Single-protein spin resonance spectroscopy under ambient conditions,” *Science* **347**, 1135 (2015).
- ²⁰C. Abeywardana, V. Stepanov, F. H. Cho, and S. Takahashi, “Electron spin resonance spectroscopy of small ensemble paramagnetic spins using a single nitrogen-vacancy center in diamond,” *J. Appl. Phys.* **120**, 123907 (2016).
- ²¹F. Dolde, H. Fedder, M. W. Doherty, T. Nöbauer, F. Rempp, G. Balasubramanian, T. Wolf, F. Reinhard, L. C. L. Hollenberg, F. Jelezko, and J. Wrachtrup, “Electric-field sensing using single diamond spins,” *Nat. Phys.* **7**, 459 (2011).
- ²²A. Jarmola, V. M. Acosta, K. Jensen, S. Chemerisov, and D. Budker, “Temperature- and magnetic-field-dependent longitudinal spin relaxation in nitrogen-vacancy ensembles in diamond,” *Phys. Rev. Lett.* **108**, 197601 (2012).
- ²³J. Cai, F. Jelezko, and M. Plenio, “Hybrid sensors based on colour centres in diamond and piezoactive layers,” *Nat. Commun.* **5**, 4065 (2014).
- ²⁴T. Fujisaku, R. Tanabe, S. Onoda, R. Kubota, T. F. Segawa, F. T.-K. So, T. Ohshima, I. Hamachi, M. Shirakawa, and R. Igarashi, “pH nanosensor using electronic spins in diamond,” *ACS Nano* **13**, 11726 (2019).
- ²⁵J. M. Taylor, P. Cappellaro, L. Childress, L. Jiang, D. Budker, P. R. Hemmer, A. Yacoby, R. Walsworth, and M. D. Lukin, “High-sensitivity diamond magnetometer with nanoscale resolution,” *Nat. Phys.* **4**, 810 (2008).
- ²⁶R. De Sousa, “Dangling-bond spin relaxation and magnetic $1/f$ noise from the amorphous-semiconductor/oxide interface: Theory,” *Phys. Rev. B* **76**, 245306 (2007).
- ²⁷J. Tisler, G. Balasubramanian, B. Naydenov, R. Kolesov, B. Grotz, R. Reuter, J.-P. Boudou, P. A. Curmi, M. Sennour, A. Thorel, *et al.*, “Fluorescence and spin properties of defects in single digit nanodiamonds,” *ACS Nano* **3**, 1959 (2009).

- ²⁸X. Song, J. Zhang, F. Feng, J. Wang, W. Zhang, L. Lou, W. Zhu, and G. Wang, “A statistical correlation investigation for the role of surface spins to the spin relaxation of nitrogen vacancy centers,” *AIP Adv.* **4**, 047103 (2014).
- ²⁹B. A. Myers, A. Das, M. Dartiailh, K. Ohno, D. D. Awschalom, and A. B. Jayich, “Probing surface noise with depth-calibrated spins in diamond,” *Phys. Rev. Lett.* **113**, 027602 (2014).
- ³⁰T. Rosskopf, A. Dussaux, K. Ohashi, M. Loretz, R. Schirhagl, H. Watanabe, S. Shikata, K. M. Itoh, and C. Degen, “Investigation of surface magnetic noise by shallow spins in diamond,” *Phys. Rev. Lett.* **112**, 147602 (2014).
- ³¹B. Ofori-Okai, S. Pezzagna, K. Chang, M. Loretz, R. Schirhagl, Y. Tao, B. Moores, K. Groot-Berning, J. Meijer, and C. Degen, “Spin properties of very shallow nitrogen vacancy defects in diamond,” *Phys. Rev. B* **86**, 081406 (2012).
- ³²K. Iakoubovskii, M. Baidakova, B. Wouters, A. Stesmans, G. Adriaenssens, A. Y. Vul, and P. Grobet, “Structure and defects of detonation synthesis nanodiamond,” *Diam. Relat. Mater.* **9**, 861 (2000).
- ³³A. Shames, A. Panich, W. a. Kempinski, A. Alexenskii, M. Baidakova, A. Dideikin, V. Y. Osipov, V. Siklitski, E. Osawa, M. Ozawa, *et al.*, “Defects and impurities in nanodiamonds: EPR, NMR and TEM study,” *J. Phys. Chem. Solids* **63**, 1993 (2002).
- ³⁴A. Soltamova, I. Ilyin, P. Baranov, A. Y. Vul, S. Kidalov, F. Shakhov, G. Mamin, S. Orlinskii, N. Silkin, and M. K. Salakhov, “Detection and identification of nitrogen defects in nanodiamond as studied by EPR,” *Physica B Condens. Matter* **404**, 4518 (2009).
- ³⁵M. Dubois, K. Guérin, E. Petit, N. Batische, A. Hamwi, N. Komatsu, J. Giraudet, P. Pirotte, and F. Masin, “Solid-state NMR study of nanodiamonds produced by the detonation technique,” *J. Phys. Chem. C* **113**, 10371 (2009).
- ³⁶Z. Peng, T. Biktagirov, F. H. Cho, U. Gerstmann, and S. Takahashi, “Investigation of near-surface defects of nanodiamonds by high-frequency EPR and DFT calculation,” *J. Chem. Phys.* **150**, 134702 (2019).
- ³⁷B. A. Myers, A. Das, M. C. Dartiailh, K. Ohno, D. D. Awschalom, and A. C. Bleszynski Jayich, “Probing surface noise with depth-calibrated spins in diamond,” *Phys. Rev. Lett.* **113**, 027602 (2014).
- ³⁸R. Tsukahara, M. Fujiwara, Y. Sera, Y. Nishimura, Y. Sugai, C. Jentgens, Y. Teki, H. Hashimoto, and S. Shikata, “Removing non-size-dependent electron spin decoherence of nanodiamond quantum sensors by aerobic oxidation,” *ACS Appl. Nano Mater.* **2**, 3701 (2019).

- ³⁹V. Stepanov and S. Takahashi, “Determination of nitrogen spin concentration in diamond using double electron-electron resonance,” *Phys. Rev. B* **94**, 024421 (2016).
- ⁴⁰F. H. Cho, V. Stepanov, and S. Takahashi, “A high-frequency electron paramagnetic resonance spectrometer for multi-dimensional, multi-frequency, and multi-phase pulsed measurements,” *Rev. Sci. Instrum.* **85**, 075110 (2014).
- ⁴¹F. H. Cho, V. Stepanov, C. Abeywardana, and S. Takahashi, “230/115 GHz electron paramagnetic resonance/double electron–electron resonance spectroscopy,” in *Methods Enzymol.*, Vol. 563 (Elsevier, 2015) p. 95.
- ⁴²T. Gaebel, C. Bradac, J. Chen, J. Say, L. Brown, P. Hemmer, and J. Rabeau, “Size-reduction of nanodiamonds via air oxidation,” *Diam. Relat. Mater.* **21**, 28 (2012).
- ⁴³M. Wolfer, J. Biener, B. S. El-Dasher, M. M. Biener, A. V. Hamza, A. Kriele, and C. Wild, “Crystallographic anisotropy of growth and etch rates of CVD diamond,” *Diam. Relat. Mater.* **18**, 713 (2009).
- ⁴⁴F. De Theije, O. Roy, N. Van Der Laag, and W. Van Enckevort, “Oxidative etching of diamond,” *Diam. Relat. Mater.* **9**, 929 (2000).
- ⁴⁵S. Dallek, L. Kabacoff, and M. Norr, “Oxidation kinetics of type 2a natural diamond [100] and [111] surfaces by TG,” *Electrochim. Acta* **192**, 321 (1991).
- ⁴⁶L. Xie, T. X. Zhou, R. J. Stöhr, and A. Yacoby, “Crystallographic orientation dependent reactive ion etching in single crystal diamond,” *Adv. Mater.* **30**, 1705501 (2018).
- ⁴⁷Q. Sun and M. Alam, “Relative oxidation behavior of chemical vapor deposited and type II a natural diamonds,” *J. Electrochem. Soc.* **139**, 933 (1992).
- ⁴⁸Z. Wenjun, Z. Fangqing, W. Quanzhong, and C. Guanghua, “Study of influence of annealing on defects in diamond films with ESR and IR measurements,” *Mater. Lett.* **15**, 292 (1992).
- ⁴⁹E. Reynhardt, G. High, and J. Van Wyk, “Temperature dependence of spin-spin and spin-lattice relaxation times of paramagnetic nitrogen defects in diamond,” *J. Chem. Phys.* **109**, 8471 (1998).
- ⁵⁰S. Steinert, F. Ziem, L. Hall, A. Zappe, M. Schweikert, N. Götz, A. Aird, G. Balasubramanian, L. Hollenberg, and J. Wrachtrup, “Magnetic spin imaging under ambient conditions with sub-cellular resolution,” *Nat. Commun.* **4**, 1607 (2013).